

Kinematically complete study of low-energy electron-impact ionization of argon: Internormalized cross sections in three-dimensional kinematics

Xueguang Ren,¹ Sadek Amami,² Oleg Zatsarinny,³ Thomas Pflüger,¹ Marvin Weyland,^{1,4} Alexander Dorn,¹ Don Madison,² and Klaus Bartschat³

¹Max Planck Institut für Kernphysik, 69117 Heidelberg, Germany

²Physics Department, Missouri University of Science and Technology, Rolla, Missouri 65409, USA

³Department of Physics and Astronomy, Drake University, Des Moines, Iowa 50311, USA

⁴Physikalisch-Technische Bundesanstalt, 38116 Braunschweig, Germany

(Received 15 February 2016; published 13 June 2016)

As a further test of advanced theoretical methods to describe electron-impact single-ionization processes in complex atomic targets, we extended our recent work on Ne($2p$) ionization [X. Ren, S. Amami, O. Zatsarinny, T. Pflüger, M. Weyland, W. Y. Baek, H. Rabus, K. Bartschat, D. Madison, and A. Dorn, *Phys. Rev. A* **91**, 032707 (2015)] to Ar($3p$) ionization at the relatively low incident energy of $E_0 = 66$ eV. The experimental data were obtained with a reaction microscope, which can cover nearly the entire 4π solid angle for the secondary electron emission. We present experimental data for detection angles of 10, 15, and 20° for the faster of the two outgoing electrons as a function of the detection angle of the secondary electron with energies of 3, 5, and 10 eV, respectively. Comparison with theoretical predictions from a B -spline R -matrix (BSR) with pseudostates approach and a three-body distorted-wave (3DW) approach, for detection of the secondary electron in three orthogonal planes as well as the entire solid angle, shows overall satisfactory agreement between experiment and the BSR results, whereas the 3DW approach faces difficulties in predicting some of the details of the angular distributions. These findings are different from our earlier work on Ne($2p$), where both the BSR and 3DW approaches yielded comparable levels of agreement with the experimental data.

DOI: [10.1103/PhysRevA.93.062704](https://doi.org/10.1103/PhysRevA.93.062704)

I. INTRODUCTION

Electron-impact ionization of atoms and molecules is of fundamental importance in both basic science and a wide variety of applications, including but not limited to modeling the physics and chemistry of planetary atmospheres, the interpretation of astrophysical data, optimizing the energy transport in reactive plasmas, and understanding as well as ultimately utilizing the effect of ionizing radiation on biological tissue in medical applications.

The full information about the ionization dynamics can be obtained in kinematically complete experiments, or so-called ($e, 2e$) studies [1,2], which determine the momentum vectors of all free particles. Moreover, in recent years experimental techniques were developed that allow one to simultaneously access a large fraction of the entire solid angle and a large range of energies of the continuum electrons in the final state [3,4]. Such experiments serve as a powerful tool to comprehensively test theoretical models that account for the quantum-mechanical few-body interactions. In recent years, theory has made tremendous progress in describing the electron-impact ionization dynamics of atomic hydrogen and helium, as well as targets such as the light alkali and alkaline-earth elements. When it comes to ionization of the outermost valence electron, these systems can usually be well described as quasi-one- and quasi-two-electron targets with an inert core.

Much more challenging, however, is the treatment of more complex targets, such as the heavy noble gases Ne – Xe [5–15]. In recent years, we measured the ionization of Ne($2p$) [5,6] and Ar($3p$) [7,8]. For Ne($2p$), unprecedented agreement between experiment and predictions from a B -spline R -matrix (BSR) with pseudostates approach was obtained first for a

projectile energy of 100 eV [5] and most recently also for the even lower energy of 65 eV [6]. While other theoretical models pretty much failed, a three-body distorted-wave (3DW) approach [9–12] also did very well in comparison with experiment for the latter case. This suggested the importance of accounting for the postcollision interaction (PCI) at such low energies of both outgoing electrons.

Regarding Ar($3p$), the comparison between experiment and the BSR predictions improved dramatically after a cross-normalization error in the processing of the experimental raw data was discovered [16,17]. For the higher incident projectile energy of 200 eV and asymmetric energy sharing between the two outgoing electrons, relatively good agreement was also achieved between experiment and a hybrid theory, which described the projectile by a distorted-wave and the initial bound state as well as the ejected-electron–residual-ion interaction by a close-coupling expansion [18,19]. For 71-eV incident energy, however, the hybrid method was inappropriate. Furthermore, the normalization correction alone did not bring completely satisfactory agreement between experiment and the BSR predictions either.

The purpose of the present study, therefore, was twofold. First, after learning many lessons from the Ne($2p$) experiments, not only regarding the proper cross normalization but also the need for setting narrow energy and angular acceptance windows of the detectors, a new set of benchmark data for an even lower incident energy (66 eV) was to be generated. Experimentally, this was achieved with further improvements on the reaction microscope and the data processing procedure. Second, it seemed important to investigate whether the success of the 3DW approach for Ne($2p$) [6] would hold up also in the case of Ar($3p$). In fact, in light of the remaining discrepancies between experiment and the BSR results for Ar($3p$) at 71 eV

[17], it was hoped that a second successful theory might provide additional clues for mutual improvement.

Ar($3p$) ionization was also studied by the Lohmann group in the coplanar asymmetric geometry, in particular at $E_0 = 113.5$ eV [20–22] using a conventional ($e, 2e$) spectrometer. In their more recent studies, a magnetic angle changer enabled the observation of the entire angular range for the slow ejected electron within the scattering plane. The same coplanar asymmetric geometry was studied by Amami *et al.* [23] at $E_0 = 200$ eV. Murray and coworkers [24,25] observed collisions with equal energy sharing of both outgoing electrons from near threshold to intermediate energies and from the coplanar to the perpendicular plane geometry.

This paper is organized as follows. After a brief description of the experimental apparatus in Sec. II, we summarize the essential points of the two theoretical models in Sec. III. The results are presented and discussed in Sec. IV, before we finish with the conclusions. Unless specified otherwise, atomic units (a.u.) are used throughout.

II. EXPERIMENT

Experiments were performed with an advanced reaction microscope [3] that was specially built for electron-impact ionization studies as drawn in Fig. 1. It was recently updated with a newly designed pulsed photoemission electron gun and a pulsed electric ion-extraction field for better ion-detection efficiency [26,27]. Since details of the experimental setup can be found in [3,26,27], only a brief outline will be given here. The well-focused (≈ 1 mm diameter) pulsed electron beam with an energy of $E_0 = 66$ eV is crossed with a continuous supersonic argon gas jet, which is produced using a $30\text{-}\mu\text{m}$ nozzle and two-stage supersonic gas expansion. The electron beam is generated by illuminating a tantalum photocathode with a pulsed ultraviolet laser beam ($\lambda = 266$ nm, $\Delta t < 0.5$ ns). The energy and temporal width of the electron pulses are about 0.5 eV (ΔE_0) and 0.5 ns (Δt_0), respectively.

Homogeneous magnetic and electric fields guide electrons (spiral lines in Fig. 1) and ions (dotted line) from the reaction volume onto two position- and time-sensitive microchannel plate detectors that are equipped with fast multihit delay-line readout. By measuring the time of flight and the impact

position for each particle their vector momenta after the collision are determined. The projectile beam axis (defining the longitudinal z direction) is aligned parallel to the electric and magnetic extraction fields. Therefore, after crossing the target gas jet, the unscattered primary beam (dashed line) reaches the center of the electron detector, where a central bore in the multichannel plates allows it to pass without inducing a signal. The detection solid angle for recoil Ar^+ ions is 4π . The acceptance angle for detection of electrons up to an energy of 15 eV is also close to 4π , except for the acceptance holes at small forward and backward angles where the electrons end up in the detector bore.

Single ionization is recorded by triple-coincidence detection of two electrons (e_1 and e_2) and the recoil ion. Therefore, two electrons arriving within a short-time interval have to be individually registered with the electron detector. Since we consider asymmetric energy sharing and forward scattering for the faster electron in the present work, the times of flight of both electrons always differ by more than 20 ns. Consequently, detector and electronic dead times do not affect our data acquisition.

In our experiment, data are recorded in a single run by the list mode (event-by-event) data acquisition. The three-dimensional momentum vectors and, consequently, kinetic energies and emission angles of final-state electrons and ions are determined from the individually measured time of flight and position in the offline data analysis. Since the complete experimentally accessible phase space is measured simultaneously, all relative data are cross-normalized and only a single global factor is required in comparison of theory and experiment [5,6].

Compared to earlier experiments [8,17], we significantly improved the electron momentum resolution of the spectrometer by increasing the homogeneity of the extraction fields and reducing the time-of-flight uncertainty due to the shorter projectile pulses. This improvement manifests itself in the resolution for the electron binding energy ($E_B = E_0 - E_1 - E_2$), for which we achieved $\Delta E_B \approx 2.0$ eV. This is about a factor of 3 better than before.

Consequently, as suggested in Ref. [28], the intervals of scattering angles $\Delta\theta_1$ and ejected electron energies ΔE_2 , over which the experimental data are integrated, were narrowed in the present work in order to reduce the resulting uncertainties in the cross-section values. The individual acceptance intervals employed in the experimental data analysis were $\theta_1 = -10 \pm 1$, -15 ± 1 , and $-20 \pm 2^\circ$ for the detection angle θ_1 of the fast outgoing electron. For the slow outgoing electron, the windows for the energy resolution were set as $E_2 = 3 \pm 1$, 5 ± 1 , and $10 \text{ eV} \pm 1 \text{ eV}$, while the angular resolution was $\Delta\theta_2 = \pm 3^\circ$ and $\Delta\phi_2 = \pm 3^\circ$. As a result, we see for some kinematical conditions that angular emission maxima and minima become better resolved in the experimental cross-section data compared to our earlier measurement [8,17]. This will be further elucidated below.

III. THEORETICAL MODELS

We used two theoretical methods to describe the present electron-impact ionization process. Although they have been described previously, we summarize the essential ideas and

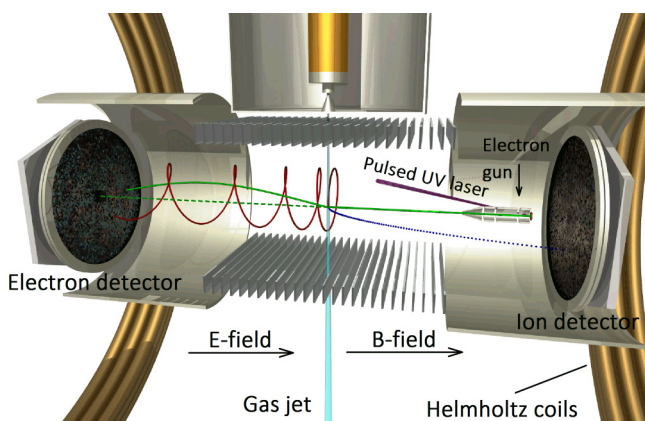


FIG. 1. Schematic view of the employed reaction microscope for electron-scattering experiments.

the particular ingredients for the current cases of interest in order to make this paper self-contained. More more detailed information can be found in the references given.

A. BSR

The BSR method (see [29] for a detailed summary and an overview of various applications) and the accompanying computer code [30] were originally developed as an alternative to the well-known R -matrix approach developed by Burke and collaborators in Belfast. An extensive description of the latter can be found in [31]. In order to allow for calculations of electron-impact ionization processes, the BSR method, like the Belfast implementation, was extended by introducing a large number of pseudostates. This became known as the R -matrix-with-pseudostates (RMPS) approach [32]. Regarding the basic idea, it is equivalent to the “convergent close-coupling” (CCC) approach developed by Bray and coworkers (see [33] for a recent review). Most importantly, the effect of the countable infinite number of high-lying Rydberg states and the uncountable infinite ionization continuum in the close-coupling expansion is approximated by a large (but finite) number of compact, and hence box-normalizable, pseudostates.

After the pseudostate close-coupling methods turned out to be extremely successful in the description of transitions between discrete physical bound states, without significant modifications needed to generate the results of interest for such

transitions, the question became how to potentially extract results for the ionization process. While the total ionization cross section for a given initial state could be obtained in a straightforward way by just adding up the excitation cross sections for all transitions from this state to pseudostates with energies above the ionization threshold, the situation is much more complicated if cross sections that are differential in energy and/or angle are required.

Details and further references to the original papers can be found in the reviews mentioned above. Here we briefly repeat how the physical *ionization* cross sections are obtained from the *excitation* amplitudes for the pseudostates [34]. To begin with, we are interested in the ionization amplitude

$$f(L_0 M_0 S_0 M_{S_0}, \mathbf{k}_0 \mu_0 \rightarrow L_f M_f S_f M_{S_f}, \mathbf{k}_1 \mu_1, \mathbf{k}_2 \mu_2) \quad (1)$$

for an initial target state with orbital angular momentum L_0 and spin S_0 (with projections M_0 and M_{S_0} , respectively) leading to a final ionic state with corresponding quantum numbers labeled by the subscript f , by an electron with initial linear momentum \mathbf{k}_0 and spin projection μ_0 resulting in two outgoing electrons described by \mathbf{k}_1, μ_1 and \mathbf{k}_2, μ_2 . We obtain this *ionization* amplitude by projecting the *excitation* amplitudes for the pseudostates (superscript p),

$$\begin{aligned} & f^p(L_0 M_0 S_0 M_{S_0}, \mathbf{k}_0 \mu_0 \rightarrow L M S M_S, \mathbf{k}_1 \mu_1) \\ &= \sqrt{\frac{\pi}{k_0 k_1}} \sum_{l_0, l_1, L_T, S_T, \Pi_T, M_{L_T}, M_{S_T}} i^{(l_0 - l_1)} \sqrt{(2l_0 + 1)} (L_0 M_0, l_0 0 | L_T M_{L_T}) (L M, l_1 m_1 | L_T M_{L_T}) \\ & \times \left(S_0 M_{S_0}, \frac{1}{2} \mu_0 | S_T M_{S_T} \right) \left(S M_S, \frac{1}{2} \mu_1 | S_T M_{S_T} \right) T_{l_0 l_1}^{L_T S_T \Pi_T} (\alpha_0 L_0 S_0 \rightarrow \alpha L S) Y_{l_1 m_1}(\theta_1, \varphi_1), \end{aligned} \quad (2)$$

to the true continuum functions for electron scattering from the residual ion, $\Psi_{L_f M_f S_f M_{S_f}}^{k_2 \mu_2 (-)}$, and summing over all energetically accessible pseudostates using the ansatz

$$\begin{aligned} & f(L_0 M_0 S_0 M_{S_0}, \mathbf{k}_0 \mu_0 \rightarrow L_f M_f S_f M_{S_f}, \mathbf{k}_1 \mu_1, \mathbf{k}_2 \mu_2) \\ &= \sum_p \langle \Psi_{L_f M_f S_f M_{S_f}}^{k_2 \mu_2 (-)} | \Phi^p(n l n' l', L S) \rangle f^p(L_0 M_0 S_0 M_{S_0}, \mathbf{k}_0 \mu_0 \rightarrow L M S M_S, \mathbf{k}_1 \mu_1). \end{aligned} \quad (3)$$

In this multichannel generalization of Eq. (15) proposed by Bray and Fursa [35], $T_{l_0 l_1}^{L_T S_T \Pi_T} (\alpha_0 L_0 S_0 \rightarrow \alpha_1 L_1 S_1)$ is an element of the T matrix for a given L_T , total spin S_T , and parity Π_T of the collision system. Choosing the z axis along the direction of the incident beam simplifies the formula to $m_0 = 0$ for the orbital angular momentum projection of the incident electron.

As seen from Eq. (3), the above procedure requires the overlap factors $\langle \Psi_{L_f M_f S_f M_{S_f}}^{k_2 \mu_2 (-)} | \Phi^p(n l n' l', L S) \rangle$ between the true continuum states and the corresponding pseudostates. The continuum states, which describe electron scattering from the residual ion, are once again obtained using the R -matrix method, with the *same* close-coupling expansion that is employed for generating the bound pseudostates. This is a critical issue, since it allows for the preservation of the crucial channel information through the projection.

Finally, the fully differential cross section (FDCS) is given by

$$\frac{d\sigma}{d\Omega_1 dE_1 d\Omega_2 dE_2} = \frac{k_1 k_2}{k_0} |f(L_0 M_0 S_0 M_{S_0}, \mathbf{k}_0 \mu_0 \rightarrow L_f M_f S_f M_{S_f}, \mathbf{k}_1 \mu_1, \mathbf{k}_2 \mu_2)|^2, \quad (4)$$

where E_i, Ω_i ($i = 1, 2$) denote the energy and the solid-angle element for detection of the two electrons.

For the present work, we started with multiconfigurations expansions of the three ionic states $(3s^23p^5)^2P^o$, $(3s3p^6)^2S$, and $(3s^23p^43d)^2S$ of Ar^+ . These states were generated by the B -spline box-based close-coupling method [36] inside a box of radius $a = 28 a_0$, where $a_0 = 0.529 \times 10^{-10}$ m denotes the Bohr radius. The one-electron orbitals were expanded in a B -spline basis and then used as the core basis to construct 482 states of neutral argon by adding another electron. All one-electron orbitals that made up these states were forced to vanish at the box boundary.

The number of physical states that can be generated by this method depends on the radius of the R -matrix (B -spline) box. The physical states are those that fit into the box with a sufficiently well-decreasing exponential tail, while the pseudostates are pushed up in energy due to the forced number of nodes within the box. It is also worth noting that the one-electron orbitals with the same value of the angular momentum are not forced to be orthogonal to each other in the BSR implementation, nor to the continuum orbitals used for the expansion of the scattering wave function inside the R -matrix box in the subsequent collision calculation. This leads to additional complexities in setting up and diagonalizing the Hamiltonian matrix, but it also has many practical advantages [29]. In particular, releasing the orthogonality restriction provides high flexibility in the description of complex targets with strong term dependence of the one-electron orbitals. In the present work, the 482 states had coupled orbital angular momenta $L \leq 5$ and energies reaching up to 80 eV.

We then performed a nonrelativistic calculation for e -Ar collisions with all 482 states included in the close-coupling expansion. The resulting equations were solved with a parallelized version of the BSR suite of computer codes [30]. Contributions from target+projectile symmetries with coupled orbital angular momenta up to 25 were included in the partial-wave expansion. The model contained up to 1445 scattering channels, leading to generalized eigenvalue problems with matrix dimensions up to 90 000 in the B -spline basis. This calculation yields scattering amplitudes for excitation of all physical and pseudostates. The amplitudes for the latter are finally projected to the true e - Ar^+ collision states for the ejected electron to obtain the ionization amplitudes. As mentioned above, in order to keep this projection consistent, it is crucial to employ the same close-coupling expansion, in our case involving the three states of Ar^+ mentioned above, that was used to generate the target states in the first place.

As a final remark, RMPS methods in general contain the full correlations, including the postcollision interaction, between all electrons involved within the R -matrix box, similarly to the CCC implementation that also employs orbitals of finite range. Hence, the size of the R -matrix box is not solely determined by the range of the discrete target states for which transitions should be described, but also by the goal of accounting as much as possible for the long-range correlations between the two electrons that can get far away from the target nucleus, i.e., the projectile and the “ejected” electron, even though the latter can actually not reach the detector in the original theoretical formulation. In principle, the dependence of the results on the box size could be tested, but in reality such tests are limited by the available computational resources. However, practitioners of the pseudostate close-coupling approach have gained much

experience over the past two decades regarding the choice of appropriate parameters.

B. The 3DW approximation

Since the details of the 3DW approximation have been outlined before [9–12], only an overview will be given here. In the 3DW approximation, the direct T matrix is given by

$$T_{\text{dir}}^{3\text{DW}} = \langle \Psi_f | W | \Psi_i \rangle. \quad (5)$$

For ionization of an atom, the initial-state wave function Ψ_i is approximated as a product of the initial Hartree-Fock bound-state wave function ψ_{HF} for the target and a distorted-wave function χ_0 for the incoming electron (the projectile):

$$\Psi_i = \psi_{\text{HF}} \chi_0. \quad (6)$$

The perturbation (W) is given by

$$W = V_i - U_i. \quad (7)$$

Here V_i is the interaction between the incident electron and the atom, while U_i is the initial-state spherically symmetric static approximation for V_i , which asymptotically approaches zero. The final-state wave function is approximated as a product of two final-state continuum electron distorted waves (χ_1 for the scattered and χ_2 for the ejected electron, respectively), and the Coulomb interaction between the outgoing electrons (C_{12}), normally called PCI:

$$\Psi_f = \chi_1 \chi_2 C_{12}. \quad (8)$$

In the 3DW approximation, we incorporate the exact electron-electron Coulomb interaction between the two electrons for C_{12} , which requires the evaluation of a six-dimensional numerical integral. This factor is a product of a Γ factor and a hypergeometric function [6]. Finally, the direct 3DW T matrix becomes

$$T_{\text{dir}}^{3\text{DW}} = \langle \chi_1 \chi_2 C_{12} | V_i - U_i | \psi_{\text{HF}} \chi_0 \rangle. \quad (9)$$

The exchange T matrix $T_{\text{exc}}^{3\text{DW}}$ is identical to Eq. (5), except that the scattered and ejected electrons are exchanged in the final-state wave function Ψ_f .

Finally, the FDCS can be written for the T matrix in atomic units as

$$\text{FDCS} = \frac{1}{(2\pi)^5} \frac{k_1 k_2}{k_0} (|T_{\text{dir}}|^2 + |T_{\text{exc}}|^2 + |T_{\text{dir}} - T_{\text{exc}}|^2), \quad (10)$$

where k_0 , k_1 , and k_2 are the magnitudes of the momenta of the initial, scattered, and ejected electrons, respectively.

Calculations are typically classified in terms of orders of perturbation theory. However, this classification can become ambiguous, since any physics contained in the approximate wave function is contained to all orders of perturbation theory, while the physics contained in the perturbation will be contained to the order of the calculation. For the 3DW approximation, the electron-electron interaction is contained in the approximate final-state wave function; hence, this physics is contained to all orders of perturbation theory. As mentioned above, the nonperturbative BSR calculation also accounts for PCI to all orders of perturbation theory, but only within the R -matrix box. In BSR calculations for ionization, therefore, the box size is generally chosen larger than required by the

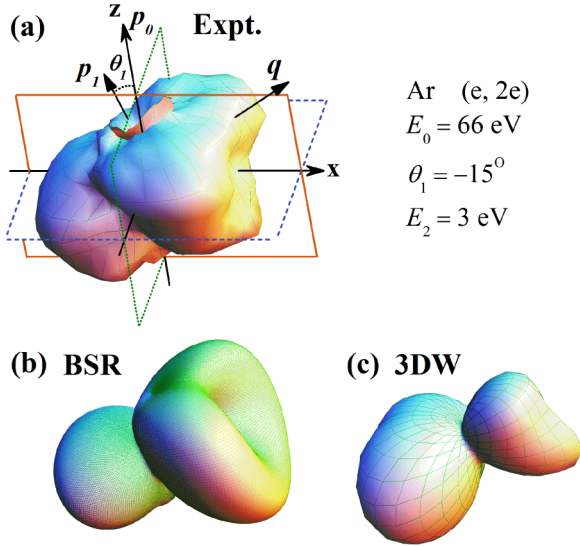


FIG. 2. Experimental and theoretical FDCS for ionization of Ar($3p$) by incident electrons with energy $E_0 = 66$ eV, presented as 3D images. The scattering angle is $\theta_1 = -15^\circ$, and the ejected electron energy is $E_2 = 3$ eV. Panel (a) shows the experimental 3D FDCS, while panels (b) and (c) represent the predictions from the BSR and 3DW theories, respectively.

typical rule [31] that exchange between the projectile electron and the target electrons is negligible.

IV. RESULTS AND DISCUSSION

Figure 2 exhibits the experimental and theoretical FDCSs for ionization of Ar($3p$) by 66-eV electron impact as three-dimensional polar plots for a projectile scattering angle of $\theta_1 = -15^\circ$ as a function of the emission direction of a slow ejected electron with $E_2 = 3$ eV energy. Panel (a) corresponds to the experimental data, while panels (b) and (c) show the calculated results from the BSR and 3DW theories, respectively. The projectile enters from the bottom and is scattered to the left (hence the minus in the notation for the angle). These two vectors define the scattering (xz) plane, as marked by the solid frame in panel (a). The momentum transfer to the target is indicated by the arrow labeled q .

In these 3D plots, the FDCS for a particular direction is given as the distance from the origin of the plot to the point on the surface, which is intersected by the ejected electron's emission direction. (Below we follow the common notation of referring to the slower of the two outgoing electrons as “ejected” and to the faster one as “scattered.”) The kinematics chosen displays exemplarily the principal features of the emission pattern: it is governed by the well-known binary and recoil lobes. The binary lobe is oriented roughly along the direction of the momentum transfer q , thus corresponding to electrons emitted after a single binary collision with the projectile. In the opposite direction the recoil lobe is found, where the outgoing slow electron, initially moving in the binary direction, additionally backscatters in the ionic potential. For ionization from p orbitals, the binary peak often exhibits a minimum along the momentum transfer direction. This is the result of the characteristic momentum profile of a p orbital

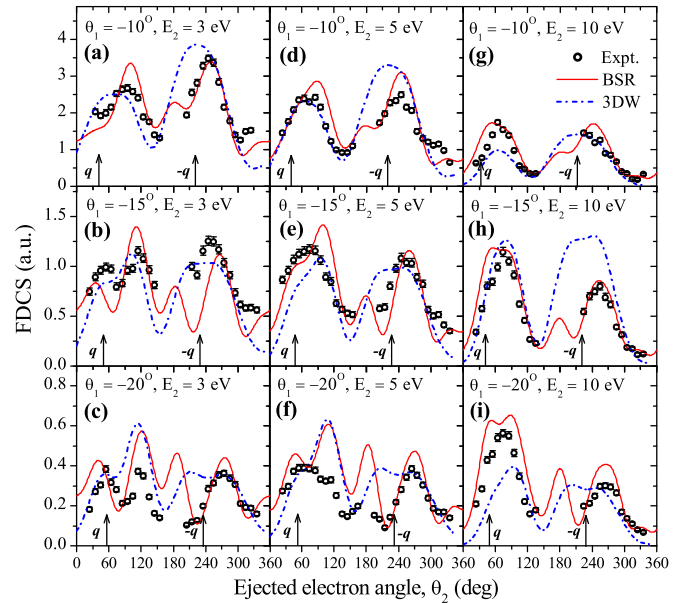


FIG. 3. FDCS for the ionization of Ar($3p$) presented as a function of the ejected electron (e_2) emission angle at scattering angles $\theta_1 = -10^\circ$ (top row), $\theta_1 = -15^\circ$ (center row), and $\theta_1 = -20^\circ$ (bottom row) for ejected-electron energies $E_2 = 3$ eV (left column), $E_2 = 5$ eV (center column), and $E_2 = 10$ eV (right column). The vertical arrows indicate the momentum transfer direction q and its opposite $-q$. The results are for the scattering plane, i.e., the xz plane of Fig. 2(a).

that has a node for vanishing momentum. Additionally, the ejected electron is repelled by the scattered projectile due to the long-range nature of the Coulomb force. These PCI effects tilt the binary and recoil lobes away from the scattered projectile direction. Furthermore, at these relatively low energies the binary lobe exhibits a much flatter shape in comparison with 3D emission patterns for high and intermediate energies.

Comparing the experimental data to the two sets of theoretical results, we see that the BSR predictions are in overall good agreement with the data. In contrast to ionization of Ne($2p$) [6] for comparable kinematical parameters, the 3DW theory underestimates the out-of-scattering-plane size of the binary peak relative to the recoil peak for the case shown.

For a more quantitative comparison between experiment and theory, the cross sections in three orthogonal planes are presented in Figs. 3–5. Those are the xz plane or scattering plane, the yz plane or half-perpendicular plane, and the xy plane or full-perpendicular plane, which are cuts through the 3D FDCS image as indicated in Fig. 2(a). The studied kinematical conditions correspond to projectile scattering angles of $\theta_1 = -10, -15$, and -20° , and to ejected electron energies of $E_2 = 3, 5$, and 10 eV, respectively. The global scaling factor used to normalize the experimental data to the theories was found by achieving a good visual fit of experiment and the BSR calculations for the FDCS in the scattering plane at $\theta_1 = -10^\circ$ and $E_2 = 3$ eV [Fig. 3(a)]. This factor was subsequently applied to all other kinematics and planes; i.e., the experimental data are consistently cross-normalized to each other.

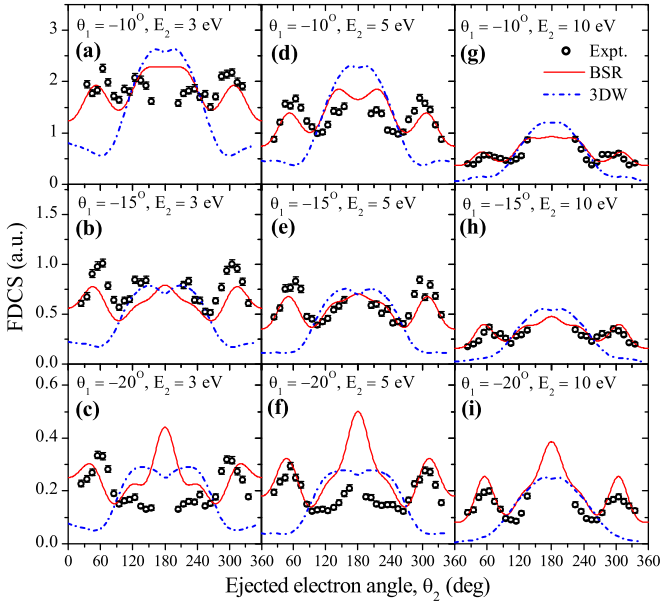


FIG. 4. Same as Fig. 3 for the “half-perpendicular” plane, i.e., the yz plane of Fig. 2(a).

Figure 3 shows a comparison between experiment and theory for detection of the secondary electron in the scattering plane. As can already be seen in the 3D plots, the BSR is in better agreement with experiment than the 3DW. Although the 3DW is in reasonably good agreement with the data for the binary peak at the smaller projectile scattering angles, it tends to predict a broader and often also higher recoil peak. The BSR, on the other hand, is in reasonably good agreement with the data, particularly for the two smaller projectile scattering angles.

For the largest projectile scattering angle and low ejected electron energies, the two theories agree better with each other

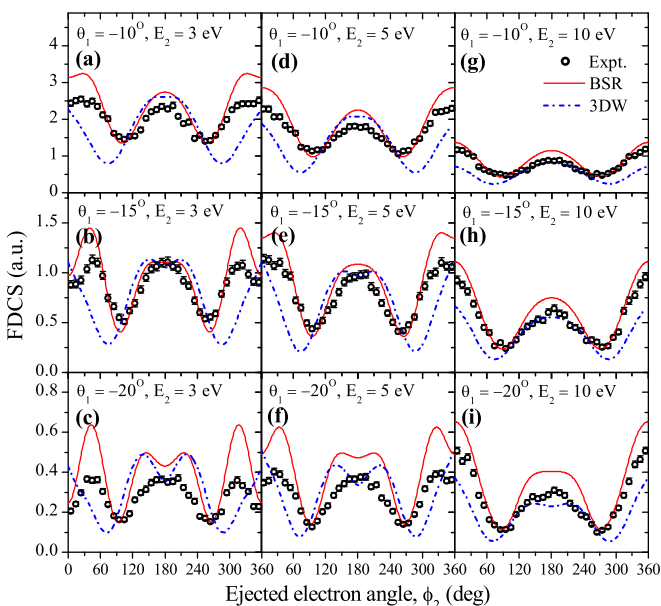


FIG. 5. Same as Fig. 3 for the “full-perpendicular” plane, i.e., the xy plane of Fig. 2(a).

than with experiment for the binary peak. As mentioned earlier, p -orbital cross sections often exhibit a double binary peak with a minimum near the momentum transfer direction. This behavior can indeed be seen in a few cases, particularly for the larger projectile scattering angles and lower energies. The BSR predicts a double recoil peak for all cases. The 3DW results exhibit a double peak only for $\theta_1 = -20^\circ$. For smaller θ_1 , it appears that these two peaks merge into a single peak. The peaks are more separated in the BSR results, with one of them being positioned near 180° . For this peak, intensity increases with increasing scattering angle. Unfortunately, the cross section close to 180° cannot be accessed experimentally. Only for $\theta_1 = -20^\circ$ and $E_2 = 5$ eV, the available data suggest a possible peak around 180° . Nevertheless, in this case as well as for $\theta_1 = -20^\circ$ and $E_2 = 3$ eV, the measured cross section in the vicinity of 180° lies significantly below the BSR predictions.

Figure 4 shows a comparison between experiment and theory for the yz plane (half-perpendicular plane). For this plane, symmetry considerations require the cross sections to be symmetric about 180° , which can indeed be seen in both theory and experiment. Here, the BSR is in much better agreement with experiment than the 3DW. Problems for the BSR remain at $\theta_1 = -20^\circ$ for $E_2 = 3$ and 5 eV. In these cases, the predicted peak at $\theta_2 = 180^\circ$ is either not seen at all or there is at best a very weak indication in the experimental data. This finding is similar to that noted above also for the scattering plane. The yz plane also reveals the too-narrow binary peak of the 3DW calculation that is already visible in the 3D plot (see Fig. 2). The 3DW binary peak is not contributing significantly to the yz -plane cross section and, consequently, all panels show that the predicted cross section is significantly smaller than observed experimentally for $\theta_2 \leq 90^\circ$ and, by symmetry, for $\theta_2 \geq 270^\circ$. As a result, the 3DW shows no indication of a binary or recoil peak in the yz plane.

Figure 5 shows the comparison between experiment and theory for the full-perpendicular plane (i.e., the xy plane). Here, the experimental angular acceptance covers the entire 0 – 360° range, but the cross sections are again symmetric with respect to 180° . The binary and recoil peaks are observed in the vicinity of $\phi_2 = 0$ and 180° , respectively. Both 3DW and BSR are in rather good agreement with the experimental data, except that the binary peaks are again too narrow in the 3DW curves. Furthermore, the 3DW does not reproduce the apparent minimum that is seen in some cases for $\phi_2 = 0^\circ$.

It is worthwhile to note that our measurements for the scattering plane are qualitatively consistent with those of the Lohmann group [20–22], which were obtained at the higher projectile energy of $E_0 = 115.5$ eV. For the projectile scattering angle $\theta_1 = -15^\circ$, for instance, we observe that with increasing ejected electron energy E_2 the two maxima of the binary peak, which are clearly visible at $E_2 = 3$ eV, merge to a single maximum at $E_2 = 10$ eV. The same behavior was reported in [20] for the same scattering angle. Furthermore, [21,22] provide some information regarding the pronounced peak at $\theta_2 = 180^\circ$ predicted by the BSR theory. For $\theta_1 = -15^\circ$, such a peak was indeed observed in the coplanar cross sections for $E_2 = 2$ eV, but it was strongly reduced and became almost invisible for $E_2 = 5$ eV. This trend is not seen in the BSR results at the present projectile energy.

We finish this section by commenting again on the improved momentum resolution of the current apparatus and the reduced angular and energy ranges that the data are summed over compared with our earlier measurement at $E_0 = 70.8$ eV [8]. Looking at the measured cross sections for corresponding kinematical cases in both experiments, it becomes clear that the overall patterns are consistent while the angular resolution is better for the present data. For the scattering plane, this can be seen by comparing Fig. 3(c) with Fig. 4(g) in [8], where the dip in the binary peak is clearly deeper in the present measurements. The same holds for the half-perpendicular plane, which was labeled “perpendicular plane” in [8]. In particular, we recommend comparing panels Figs. 4(a)–4(c) above with Figs. 4(d), 4(f), and 4(h) in [8], respectively.

V. CONCLUSIONS

We have reported a comprehensive study of the electron-impact ionization dynamics of Ar($3p$) at the relatively low incident projectile energy of 66 eV. The fully differential cross sections obtained experimentally were internormalized across three scattering angles θ_1 from -10 to -20° and three ejected electron energies E_2 from 3 to 10 eV. The present experimental data substantially enhance the still very limited set of data currently available to thoroughly test theoretical methods for describing this complex and highly correlated problem.

Overall, our experimental data and the BSR predictions agree at a similar level as in previous studies, in particular for the two smaller scattering angles $\theta_1 = -10$ and -15° , whereas the 3DW results reveal significant deviations from experiment in some cases. The latter findings are different from our recent work on Ne($2p$) ionization [6], where both BSR and 3DW yielded comparable levels of agreement with the experimental

data. It is conceivable that the energies considered in this work are too low for the 3DW approach, which does not contain channel coupling. Another possibility for the difficulties could be the fact that the current implementation of the 3DW method uses single-configuration descriptions of the initial bound and the final ionic target states, rather than the multiconfiguration expansions with term-dependent orbitals that can be employed in the BSR approach.

One of the primary strengths of the 3DW approach lies in the exact treatment of PCI. Accordingly, we find that the 3DW is in qualitative agreement with experiment concerning the angular positions of the peaks in the scattering plane, which are strongly influenced by PCI. On the other hand, the 3DW cross section in the binary regime is too small, particularly outside the scattering plane. This results in poor agreement with experiment and the BSR predictions in the half-perpendicular plane. Based on the present results, we conclude that the important physical effects determining the cross sections appear to be very different for Ne and Ar, since the 3DW was in good agreement for Ne for essentially the same kinematics.

ACKNOWLEDGMENTS

This work was supported, in part, by NSF Grants No. PHY-1505819 (S.A. and D.M.), No. PHY-1403245, and No. PHY-1520970 (O.Z. and K.B.). Supercomputer resources were provided through Grants No. TG-MCA075029 (S.A. and D.M.) and No. PHY-090031 (O.Z. and K.B.) in the eXtreme Science and Engineering Discovery Environment program of the NSF. S.A. would also like to thank the Libyan Ministry of Higher Education’s Scholarship for financial support.

-
- [1] H. Ehrhardt, M. Schulz, T. Tekaas, and K. Willmann, *Phys. Rev. Lett.* **22**, 89 (1969).
 - [2] U. Amaldi, A. Egidi, R. Marconero, and G. Pizzella, *Rev. Sci. Instrum.* **40**, 1001 (1969).
 - [3] J. Ullrich, R. Moshhammer, A. Dorn, R. Dörner, L. Schmidt, and H. Schmidt-Böcking, *Rep. Prog. Phys.* **66**, 1463 (2003).
 - [4] M. Dürr, C. Dimopoulou, A. Dorn, B. Najjari, I. Bray, D. V. Fursa, Z. Chen, D. H. Madison, K. Bartschat, and J. Ullrich, *J. Phys. B* **39**, 4097 (2006).
 - [5] T. Pflüger, O. Zatsarinny, K. Bartschat, A. Senftleben, X. Ren, J. Ullrich, and A. Dorn, *Phys. Rev. Lett.* **110**, 153202 (2013).
 - [6] X. Ren, S. Amami, O. Zatsarinny, T. Pflüger, M. Weyland, W. Y. Baek, H. Rabus, K. Bartschat, D. Madison, and A. Dorn, *Phys. Rev. A* **91**, 032707 (2015).
 - [7] X. Ren, A. Senftleben, T. Pflüger, A. Dorn, K. Bartschat, and J. Ullrich, *Phys. Rev. A* **83**, 052714 (2011).
 - [8] X. Ren, T. Pflüger, J. Ullrich, O. Zatsarinny, K. Bartschat, D. H. Madison, and A. Dorn, *Phys. Rev. A* **85**, 032702 (2012).
 - [9] A. Prideaux and D. H. Madison, *Phys. Rev. A* **67**, 052710 (2003).
 - [10] D. H. Madison and O. Al-Hagan, *J. At. Mol. Opt. Phys.* **2010**, 367180 (2010).
 - [11] S. Amami, A. Murray, A. Stauffer, K. Nixon, G. Armstrong, J. Colgan, and D. Madison, *Phys. Rev. A* **90**, 062707 (2014).
 - [12] S. Amami, A. Murray, A. Stauffer, K. Nixon, G. Armstrong, J. Colgan, and D. Madison, *Phys. Rev. A* **91**, 069906(E) (2015).
 - [13] X. Ren, A. Senftleben, T. Pflüger, A. Dorn, K. Bartschat, and J. Ullrich, *J. Phys. B* **43**, 035202 (2010).
 - [14] I. Taouil, A. Duguet, A. Lahmam-Bennani, B. Lohmann, J. Rasch, C. T. Whelan, and H. R. J. Walters, *J. Phys. B* **32**, L5 (1999).
 - [15] F. K. Miller, H. R. J. Walters, and C. T. Whelan, *Phys. Rev. A* **91**, 012706 (2015).
 - [16] X. Ren, A. Senftleben, T. Pflüger, J. Ullrich, K. Bartschat, and A. Dorn, *Phys. Rev. A* **89**, 029904(E) (2014).
 - [17] X. Ren, T. Pflüger, J. Ullrich, O. Zatsarinny, K. Bartschat, D. H. Madison, and A. Dorn, *Phys. Rev. A* **92**, 019901(E) (2015).
 - [18] K. Bartschat and P. G. Burke, *J. Phys. B* **20**, 3191 (1987).
 - [19] K. Bartschat and O. Vorov, *Phys. Rev. A* **72**, 022728 (2005).
 - [20] M. A. Haynes and B. Lohmann, *Phys. Rev. A* **64**, 044701 (2001).
 - [21] M. A. Stevenson and B. Lohmann, *Phys. Rev. A* **77**, 032708 (2008).
 - [22] L. R. Hargreaves, M. A. Stevenson, and B. Lohmann, *J. Phys. B* **43**, 205202 (2010).
 - [23] S. Amami, M. Ulu, Z. N. Ozer, M. Yavuz, S. Kazgoz, M. Dogan, O. Zatsarinny, K. Bartschat, and D. Madison, *Phys. Rev. A* **90**, 012704 (2014).

- [24] A. J. Murray, N. J. Bowring, and F. H. Read, *J. Phys. B* **33**, 2859 (2000).
- [25] K. L. Nixon, A. J. Murray, and C. Kaiser, *J. Phys. B* **43**, 085202 (2010).
- [26] X. Ren, T. Pflüger, M. Weyland, W. Y. Baek, H. Rabus, J. Ullrich, and A. Dorn, *J. Chem. Phys.* **141**, 134314 (2014).
- [27] X. Ren, E. Jabbour Al Maalouf, A. Dorn, and S. Denifl, *Nat. Commun.* **7**, 11093 (2016).
- [28] O. Zatsarinny and K. Bartschat, *Phys. Rev. A* **85**, 032708 (2012).
- [29] O. Zatsarinny and K. Bartschat, *J. Phys. B* **46**, 112001 (2013).
- [30] O. Zatsarinny, *Comput. Phys. Commun.* **174**, 273 (2006).
- [31] P. G. Burke, *R-Matrix Theory of Atomic Collisions* (Springer-Verlag, New York, 2011).
- [32] K. Bartschat, E. T. Hudson, M. P. Scott, P. G. Burke, and V. M. Burke, *J. Phys. B* **29**, 115 (1996).
- [33] I. Bray, D. Fursa, A. Kadyrov, A. Stelbovics, A. Kheifets, and A. Mukhamedzhanov, *Phys. Rep.* **520**, 135 (2012).
- [34] O. Zatsarinny and K. Bartschat, *Phys. Rev. Lett.* **107**, 023203 (2011).
- [35] I. Bray and D. V. Fursa, *Phys. Rev. A* **54**, 2991 (1996).
- [36] O. Zatsarinny and C. F. Fischer, *Comput. Phys. Commun.* **180**, 2041 (2009).